Decomposition Kinetics for HONO and HNO_2

Xi Chen[a,1], Mark E. Fuller[b,1], C. Franklin Goldsmith[b,*]

[a] *Department of Chemistry, Brown University, Providence, RI, 02912, USA*
[b] *School of Engineering, Brown University, Providence, RI, 02912, USA*

Abstract

This work presents a detailed investigation into the isomerization and decomposition of HONO and HNO_2. State-of-the-art electronic structure theory is used to compute the HNO_2 potential energy surface. Temperature and pressure dependent rate coefficients are computed using microcanonical rate theory and the master equation. The electronic structure theory properties are optimized against the relevant experimental data. A novel strategy was developed to incorporate uncertainty in the minimum energy pathway into the optimized mechanism. The new mechanism is in excellent agreement with all available experimental data for H + NO_2 → OH + NO and OH + NO → HONO. The calculations identify OH + NO as the dominant products for HNO_2, which were neglected from all previous mechanisms in the literature.

Keywords: HONO, HNO_2, nitrogen chemistry, master equation combustion

*Corresponding author: C. Franklin Goldsmith
Email address: franklin_goldsmith@brown.edu (C. Franklin Goldsmith)
[1] These authors contributed equally to this work.

1. Introduction

Nitrous acid (HONO) and its isomer nitryl hydride (HNO_2) are key intermediates in many gas-phase systems, from atmospheric chemistry to combustion to energetic materials. The most common source of these two species is through H-abstraction or disproportionation involving NO_2. Additionally, HONO can be formed via concerted elimination from various NO_2-containing functional groups, such as nitroalkanes ($C-NO_2$), alkylnitrates ($O-NO_2$), and nitroamines ($N-NO_2$). In contrast, concerted HNO_2 elimination from the analogous nitrite compounds, X−ONO, does not exist as a viable product channel, owing to the enthalpically and entropically more favorable O−NO fission.

Recent developments in advanced engines, such as exhaust gas recirculation (EGR) and the use of alkyl-nitrates as reactivity enhancers, create new environments in which NO_2 chemistry is increasingly important [1–3]. One way in which NO_2 contributes to increased reactivity (*e.g.* decreased ignition delay times) is through various radical + NO_2 reactions that shift the composition from comparatively less reactive radicals to more reactive radicals [4–6]:

$$R + NO_2 \rightleftharpoons RO + NO \tag{R1}$$

$$RO_2 + NO \rightleftharpoons RO + NO_2 \tag{R2}$$

$$RO \rightarrow\rightarrow \text{carbonyl} + \text{alkene} + H \tag{R3}$$

$$H + NO_2 \rightleftharpoons OH + NO \tag{R4}$$

An alternative pathway involves the abstraction of H from a fuel molecule:

$$RH + NO_2 \rightleftharpoons R + HONO/HNO_2 \quad \text{(R5)}$$

$$HNO_2 \rightleftharpoons HONO \quad \text{(R6)}$$

$$HONO \rightleftharpoons OH + NO \quad \text{(R7)}$$

$$HNO_2 \rightleftharpoons OH + NO \quad \text{(R8)}$$

Whereas the reaction sequence (R1-R4), is chain propagating, the reaction sequence (R5-R8) is chain branching. Recent experimental and modeling work has highlighted the sensitivity of ignition delay times to this reaction sequence for H_2, CH_4, and C_3H_8 [7–11]. One of the authors recently published rate coefficients for (R5) obtained from transition state theory (TST) calculations for a broach range of fuels.[12] The HNO_2 potential energy surface (PES), shown in Figure 1.

As seen in Figure 1, two different rotational conformers of HONO exist. The more stable rotamer, *anti*-HONO (frequently referred to as "*trans*-HONO" in the literature), is when the HO−NO dihedral angle is 180°. At present, there is little consistency in the combustion literature on whether both *anti*-HONO and *syn*-HONO should be included, or if they should be lumped into a single species. The barrier for torsional rotation between the two conformers is 44 kJ/mol (10.6 kcal/mol), which is large enough that these two species can persist as distinct at elevated temperatures. As demonstrated in Ref. 12, these two rotamers have different reactivity.

The aim of the present work is to provide an accurate analysis of the

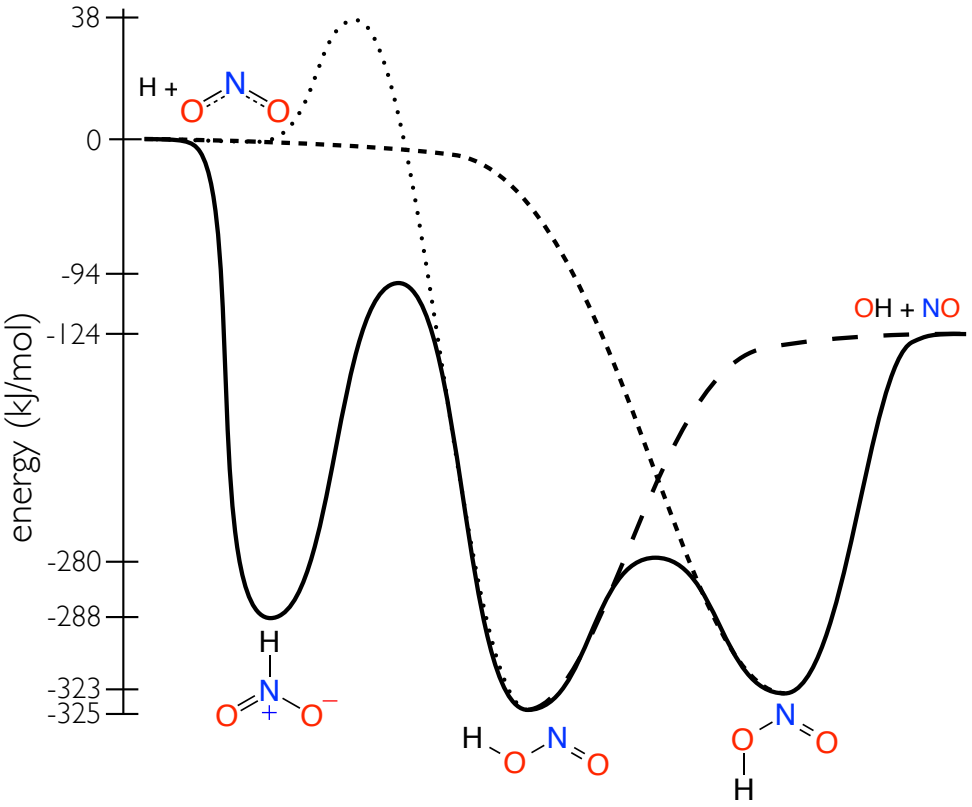

Figure 1: Potential energy diagram illustrating the major stationary points on the HNO_2 PES, energies relative to the most stable isomer.

HNO_2 potential energy surface and the kinetics of reactions (R4, R6-R8). The approach will be to use state-of-the-art methods in electronic structure theory and computational kinetics to provide temperature- and pressure-dependent rate coefficients. The electronic structure and collisional energy transfer parameters are then optimized against diverse experimental data to provide a rigorously optimized system of rate constants.

2. Methods

2.1. Electronic Structure Theory

The stationary points on the HNO_2 potential energy surface (PES) were computed using a compound method that is based upon the ANL1 schema[13]. Briefly, geometry optimization and normal mode analysis were performed using UCCSD(T)/cc-pVQZ. The optimized geometries were followed by a sequence of single-point calculations to correct for: (i) basis set extrapolation, using aug-cc-pVQZ (aqz) and aug-cc-pV5Z (a5z) basis sets, E_{CBS}; (ii) higher-order excitations that include perturbative quintuples with cc-pVDZ and cc-pVTZ basis sets, $\Delta E_{\mathrm{T/Q}}$; (iii) anharmonic corrections, based upon density functional theory calculations, ΔE_{anh}; (iv) core-valence interactions, which include the core electrons in the coupled-cluster calculations, with the cc-pcVQZ (cqz) and cc-pcV5Z (c5z) basis sets, $\Delta E_{\mathrm{c.v.}}$; and (v) relativistic effects, as estimated by the difference in the CCSD(T) energy with and without the Douglas-Kroll one-electron integrals with the aug-cc-pcVQZ-DK basis (acQZ-DK), ΔE_{rel}. The zero-point energy, ZPE, is that obtained from the UCCSD(T)/cc-pVQZ normal mode analysis. This compound method should be accurate to within $\pm$ 1.3 kJ/mol at 2σ uncertainty for local minima; for saddle points, we assume that the uncertainty is twice as high. For a more detailed discussion of these corrections and their contributions to the total energy, the reader is referred to ref. 13.

$$
\begin{aligned}
E_{\mathrm{ANL1}} &= E_{\mathrm{CBS}} + ZPE + \Delta E_{\mathrm{T/Q}} + \Delta E_{\mathrm{anh}} + \Delta E_{\mathrm{c.v.}} + \Delta E_{\mathrm{rel}} \qquad (1)\\
E_{\mathrm{CBS}} &= E_{\mathrm{UCCSD(T)/a5z}} - \frac{5^4}{6^4 - 5^4}\left(E_{\mathrm{UCCSD(T)/a5z}} - E_{\mathrm{UCCSD(T)/aqz}}\right)\\
\Delta E_{\mathrm{T/Q}} &= \left(E_{\mathrm{UCCSDT(Q)/dz}} - E_{\mathrm{UCCSD(T)/dz}}\right)\\
\Delta E_{\mathrm{anh}} &= \left(ZPE^{anh}_{\mathrm{B3LYP/6\text{-}311{+}{+}G(d,p)}} - ZPE^{harm}_{\mathrm{B3LYP/6\text{-}311{+}{+}G(d,p)}}\right)\\
\Delta E_{\mathrm{c.v.}} &= \left(E_{\mathrm{UCCSD(T,full)/CBS(cqz,\ c5z)}} - E_{\mathrm{UCCSD(T)/CBS(cqz,\ c5z)}}\right)\\
\Delta E_{\mathrm{rel}} &= \left(E_{\mathrm{UCCSD(T)/acQZ\text{-}DK}} - E_{\mathrm{DK\text{-}UCCSD(T)/acQZ\text{-}DK}}\right)
\end{aligned}
$$

As depicted in Figure 1, the H + NO_2 and the OH + NO pathways do not have first-order saddle points in potential energy. The minimum energy paths that are required for the variational transition state theory were treated using the multi-reference methods CASPT2[14–16] and MRCI+Q[17–19]. The active space in the H + NO_2 calculations was 14 electrons in 11 orbitals (14e,11o): 6 orbitals for the delocalized π-system of NO_2, 4 orbitals for the two pairs of N−O σ, σ^* in NO_2, and 1 orbital for the H atom (this active space is effectively equivalent to the complete valence space for the system, not including the two 2s orbitals for the oxygen atoms). The CASPT2 and MRCI+Q calculations were performed with aug-cc-pVQZ and aug-cc-PV5Z basis sets and extrapolated to the complete basis set limit. To further improve the accuracy of the multi-reference calculations, a separate set of potentials was computed on a higher spin surface[20–23]. The potential energy of the triplet surface was computed using both the ANL1 method of Equation (1) as well as the CASPT2 and MRCI+Q approaches. The coupled-cluster triplet surface is then added to the multi-reference singlet-triple splitting to obtain a more accurate representation of the minimum energy path on the

singlet surface:

$$^1E_{\mathrm{ANL1/MR}} = {}^3E_{\mathrm{ANL1}} + \left({}^1E_{\mathrm{MR}} - {}^3E_{\mathrm{MR}}\right) \tag{2}$$

where the superscript indicates the spin multiplicity of the surface, and "MR" implies either CASPT2 or MRCI+Q with aug-cc-pV∞Z basis sets.

The H + NO_2 pathway leading to *anti*-HONO, despite being a radical-radical reaction, has a well-defined first-order saddle point, depicted by the dotted line in Figure 1. This transition still has a strong bi-radical character, and multi-reference methods were necessary. The transition state optimization was performed using CASPT2(14e,11o)/aug-cc-pVQZ, with the same active space as above. The spin-splitting method of (2) was applied to further improve the accuracy. This local maximum is a consequence of the nodal planes in the NO_2 singularly occupied molecular orbital (SOMO); as the H atom approaches either O atom in the *anti* configuration, it experiences significant overlap with the lobes of opposite sign on the N atom on *syn* configuration of the O atoms[12].

For the OH + NO potentials, the active space was (8e,6o): 4 orbitals for the complete π system in NO and 2 orbitals for the π system in OH. The orbitals in these calculations were averaged over four states to account for the spatial degeneracy in both OH and NO on the singlet surface. Because of the low-lying excited states, single determinant methods were not reliable, and the singlet-triplet splitting approach in Equation (2) could not be applied.

All wavefunction-based calculations were performed in Molpro.[24] The density functional theory calculations used for the anharmonic correction were done in Gaussian09[25].

2.2. Computational Kinetics

Reactions (R4) and (R6)-(R8) proceed through one or more unimolecular intermediates, and thus the rate constants are a function of pressure. The temperature- and pressure-dependent rate constants are computing using the microcanonical rate theory and the master equation (RRKM/ME) code MESS[26, 27], which is part of the computational kinetics package PAPR developed by Argonne National Laboratory[28]. A single exponential was used to model the collisional energy transfer, with a preliminary value of $\langle \Delta E_{\text{down}} \rangle = 200\,(T/298[\text{K}])^{0.85}$ cm^{-1}; the pre-factor will be optimized, as described in the next section. The collision frequency is computed using a Lennard-Jones model with either He or N_2 as a collider, with $\sigma_{\text{He}} = 2.6$ Å, $\sigma_{N_2} = 3.3$ Å, $\sigma_{\text{HONO}} = 5.1$ Å, $\epsilon_{\text{He}} = 0.06$ kJ/mol, $\epsilon_{N_2} = 2.2$ kJ/mol, and $\epsilon_{\text{HONO}} = 2.0$ kJ/mol. For OH and NO, the low-lying excited states that result from spin-orbit splitting were included, with a separate energy levels of 140 cm^{-1} and 112 cm^{-1} for OH and NO, respectively.[29]

In the time-dependent master equation, the eigenvalues of the transition matrix can be separated into chemically significant eigenvalues (CSE) and internal energy relaxation eigenvalues (IERE), with the former typically smaller than the latter by several orders of magnitude[30, 31]. When a CSE approaches the smallest IERE, it indicates that a pair of wells (or a well and bimolecular products) will equilibrate on a timescale that approaches the rate of ro-vibrational energy relaxation. When this merging of timescales occurs, it no longer makes sense to think of these species as being chemically distinct in a macroscopic model[32]. An important feature of MESS is the ability to determine when two wells equilibrate rapidly (*e.g.* at high temperature) and

combine them accordingly[26].

This "well-merging" capability is important for the HNO_2 reactive system. At low temperatures, the two HONO rotamers remain chemically distinct. At higher temperatures, however, the chemically significant eigenvalue that corresponds to the interconversion between *anti*-HONO and *syn*-HONO blends into the IERE continuum. Preliminary calculations suggest that this merging occurs at 650 K and 0.01 bar, and at 800 K and 100 bar. Above these temperatures, they exist only as a single HONO. Below these temperatures, when the two rotamers are distinct, the rate constant for their interconversion is large (*e.g.* 2×10^9 s^{-1}), and they will rapidly equilibrate in the conventional sense. Precisely how species merging should be handled at high temperatures remains an open challenge in reactive flow simulations, since it represents a reduction in the number of species (and accordingly the state vector)[33]. Since our primary interest is in high-temperature kinetics, we lump these two species into a single HONO isomer. In this two-well model, with HONO and HNO_2 as distinct isomers, the interconversion between *anti*- and *syn*-HONO is treated as hindered internal rotation; the partition function was computed via summation over the energy levels for the corresponding 1D Schrödinger equation.

For the two remaining transition states with saddle points, H + NO_2 $\rightleftharpoons$ *anti*-HONO and HNO_2 $\rightleftharpoons$ *anti*-HONO, the microcanonical rate constants were computed using conventional rigid-rotor harmonic-oscillator approximations.

The transition states for the barrierless reactions are computed using Variable Reaction Coordinate Transition State Theory (VRC-TST)[34–37],

as implemented in VaReCoF in Papr[38, 39]. In VRC-TST, the internal degrees of freedom of the transition state are divided into conserved and transitional modes. The conserved modes correspond to the internal degrees of freedom of the two fragments at infinite separation. The transitional modes are the coupled, anharmonic modes that correspond to relative translation and rotation at infinite separatation and are converted into vibrational modes in the equilibrium structures. Note that one of the transitional modes is the reaction coordinate. The transitional modes are large in amplitude (if treated harmonically, they would have very low vibrational frequencies), and so these modes are treated using classical phase space theory representations[40]. The multi-dimensional partition function is evaluated via Monte Carlo sampling; the potential energy is computed on-the-fly by calling Molpro to return the CASPT2/cc-pVTZ energy for a given set of Cartesian coordinates.

A sequence of 1D corrections are included to account for geometry relaxation and basis set extrapolation. First, for a fixed bond distance r (*e.g.* N−O in OH + NO → HONO), the internal degrees of freedom for the two fragments are kept frozen at their respective equilibrium geometries, and the degrees of freedom for the relative position are relaxed at the CASPT2/cc-pVTZ level, $V_{\text{constained}}(r)$. In the next set of calculations, the internal degrees of freedom are no longer held rigid, and all degrees of freedom (apart from r) are relaxed, $V_{\text{relaxed}}(r)$. The difference in these two $V(r)$ is the 1D geometry relaxation correction. Additionally, single-point calculations are performed using larger basis sets for the fully relaxed case, which can then be used to provide a basis set correction. As will be detailed below, these 1D corrections can be manipulated to explore how the uncertainty in the interaction

potential corresponds to uncertainties in the final rate constants.

For the H + NO_2 reactions, the H atom can add to either the N or the O atoms. Within the VRC-TST methodology, the flux to these different products (HNO_2 and HONO, respectively) must be determined separately. Accordingly, a plane of infinite potential was imposed on the NO_2, normal to the plane[39, 41]. For H + $NO_2 \rightarrow HNO_2$, the plane is defined such that bonding to the O atoms is impossible, and for H + $NO_2 \rightarrow$ HONO, the plane is in the same location, but with a sign change, such that bonding to the N atom is impossible. The location of this dividing surface was optimized variationally so as to minimize the total H + NO_2 flux.

The rate constants are computed at temperatures $200 \leq T \leq 2500$ K and pressures $0.01 \leq P \leq 100$ bar.

2.3. Optimization Methodology

A key aspect of the present work is the inclusion of uncertainty in each of the model parameters. Each parameter can be adjusted within its upper and lower bound as a means of providing global uncertainty quantification. Moreover, this ensemble of models can then be compared to diverse experimental data to determine the optimum set of model parameters that best reproduce the data. This form of optimization is similar to the Multiscale Informatics (MSI) of Burke and coworkers[42–45]. Previous implementations of the MSI methodology focused on stationary points on the PES, as well as vibrational frequencies and energy transfer models. The present work is the first extension of the MSI framework to include the potential energy surface for barrierless reactions.

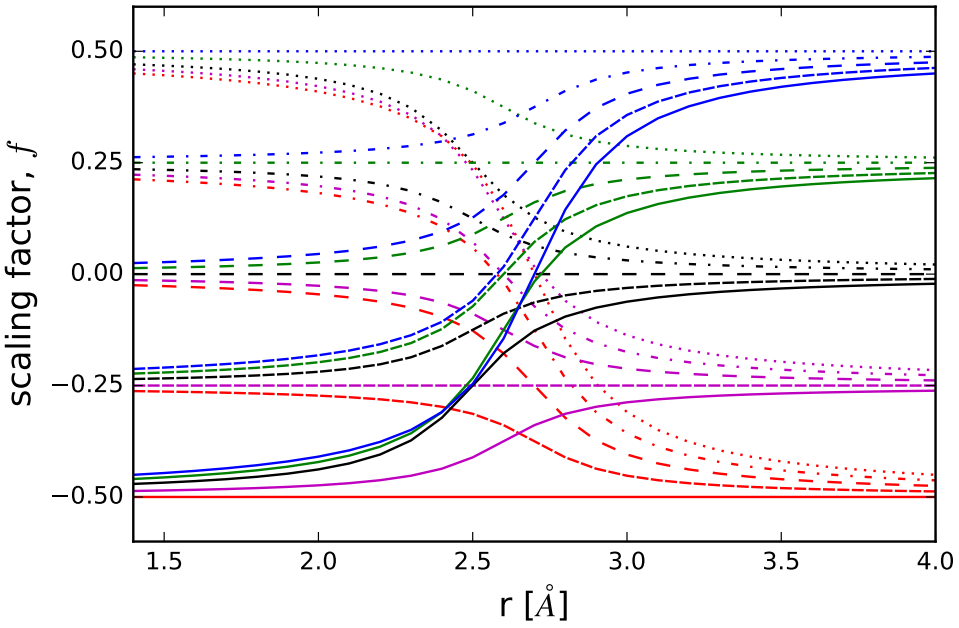

Figure 2: Scaling factors used to create an array of correction potentials.

To explore how the uncertainty in the minimum energy pathway for barrierless reactions could influence the final rate constants, a family of scaling factors, f, were created, Figure 2. Starting from the average value (the horizontal, wide-dashed black line at $f = 0.0$), the minimum energy path can be scaled down (up) to produce a curve that is more (less) attractive than the nominal case. For example, the dotted blue line at $f = 0.5$ represents an increase in the potential of 50% for all r, and the densely dashed magenta line at $f = -0.25$ represents a new potential that is more attractive by 25%. More importantly, additional curves are created that will cross the average value: some curves may be less attractive at longer distances and more attractive at shorter distances, such has the solid green line, which begins at $f = 0.25$ at $r > 4$ and limits to $f = -0.5$ at $r < 1.4$. The limits of this

switching function were chosen so that the variability is greatest over the region of the reaction coordinate where the dynamical bottleneck is mostly likely to occur; for radical-radical reactions above room temperature, the bottleneck is typically found between $-50 \leq V(r) \leq -1$ kJ/mol.

The scaled potential is given by: $V_{\text{new}}(r) = V_{\text{avg}}(r)(1 - f(r))$. These new potentials are incorporated into the VRC-TST framework as 1D correction factors: $\Delta E_{\text{1D}} = V_{\text{new}}(r) - V_{\text{constained}}(r)$. As depicted in Figure 2, since there are 25 scaling factors f, there will be 25 ΔE_{1D} to consider. In the VaReCoF calculations, a separate variational optimization is performed for each of the 25 corrections, thereby providing a unique microcanonical rate constant for each scaling factor. For H + NO_2 $\rightarrow$ HNO_2 and H + NO_2 $\rightarrow$ HONO, the average value is the arithmetic mean of the CASPT2(14e,11o)/aug-cc-PV∞Z and MRCI+Q(14e,11o)/aug-cc-PV∞Z, both with and without the spin correction of Equation (2). For OH + NO $\rightarrow$ HONO, the average value is the arithmetic mean of the CASPT2(8e,6o)/aug-cc-PV∞Z and MRCI+Q(8e,6o)/aug-cc-PV∞Z.

The MSI variables are the eight stationary points in Table 1, with the upper and lower limits as expected by the ANL1 method; the collisional energy transfer pre-factor, $100 \leq \Delta E_{down} \leq 500$ cm^{-1}, and the scaling factors, f, for H + NO_2 $\rightarrow$ HNO_2, H + NO_2 $\rightarrow$ HONO, and OH + NO $\rightarrow$ HONO.

Two sets of experimental data are used to constrain the model parameters. The first set of experiments are for the H + NO_2 $\rightarrow$ OH + NO reaction, which includes flow cell data at lower temperatures[46], high-pressure flow cells at intermediate temperatures[47], and shock tube measurements using two different diagnostics at high temperatures[48]. These data primarily

constrain the two H + NO_2 interaction potentials. The second set of experimental data are the high-pressure flow cell work by Troe and coworkers on OH + NO → HONO[49]. These data primarily constrain the OH + NO interaction potential and the collisional energy transfer coefficient, ΔE_{down}.

3. Results and Discussion

	relative energy [kJ/mol]	
Name	PW	ATcT[50]
$H + NO_2$	0.0	0.0
$OH + NO$	-124.4 ± 1.3	-125.0 ± 0.03
HNO_2	-288.0 ± 1.3	-290.0 ± 1.40
syn-HONO	-323.0 ± 1.3	-324.3 ± 0.28
anti-HONO	-324.7 ± 1.3	-325.9 ± 0.05
TS: syn-HONO ⇌ anti-HONO	-280.4 ± 2.6	
TS: HNO_2 ⇌ anti-HONO	-93.9 ± 2.6	
TS: anti-HONO ⇌ $H + NO_2$	38.4 ± 2.6	

Table 1: key stationary points on the HNO_2 potential energy surface, relative to $H + NO_2$.

The ANL1 results for the stationary points on the PES are presented in Table 1. Also included in the table are the ATcT results. The root mean square deviation between the two methods was 0.7 kJ/mol.

3.1. $H + NO_2 \rightarrow products$

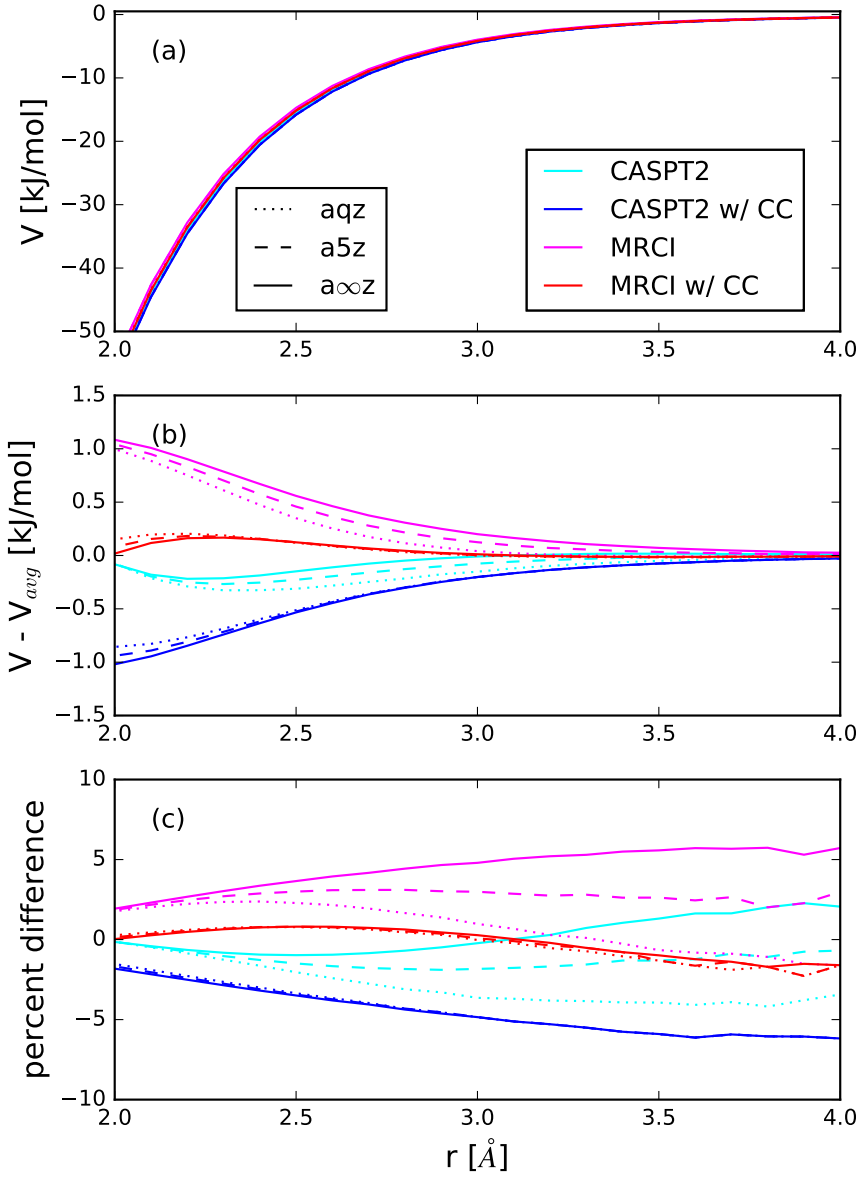

Figure 3: (a) minimum energy path between H + NO_2 and HNO_2. The colors correspond to different methods, and the line styles correspond to different basis sets. (b) difference between the potential and the average of the four methods at the aug-cc-pV∞Z limit; (c) the percent difference between the methods and the average.

The results of the H + NO_2 $\rightarrow$ HNO_2 potential are shown in Figure 3. The four colors correspond to the four different methods that were used to compute the minimum energy pathway: pure CASPT2(14e,11o), cyan; pure MRCI+Q(14e,11o), magenta; ANL1 on the triplet surface, with CASPT2(14e,11o) singlet-triplet splitting, blue; and ANL1 on the triplet surface, with MRCI+Q(14e,11o) singlet-triplet splitting, red. Each of these four methods was computed using both aug-cc-pVQZ and aug-cc-pV5Z basis sets and then extrapolated to the CBS limit.

As can be seen in the figure, all four methods are well converged with respect to the basis set. Figure 3b plots the difference between each of the four methods and the geometric mean of the four (at aug-cc-pV∞Z). Of greater significance is the percent deviation of the methods from the average, Figure 3c, since the percent deviation is a better reflection on the final uncertainty of the transition state. Note that all twelve curves agree to within 5%. In principle, it is difficult to say exactly what the "true" value for the potential is. However, given the degree of convergence, we estimate that the average value for the minimum energy path is likely within 25% of the correct value.

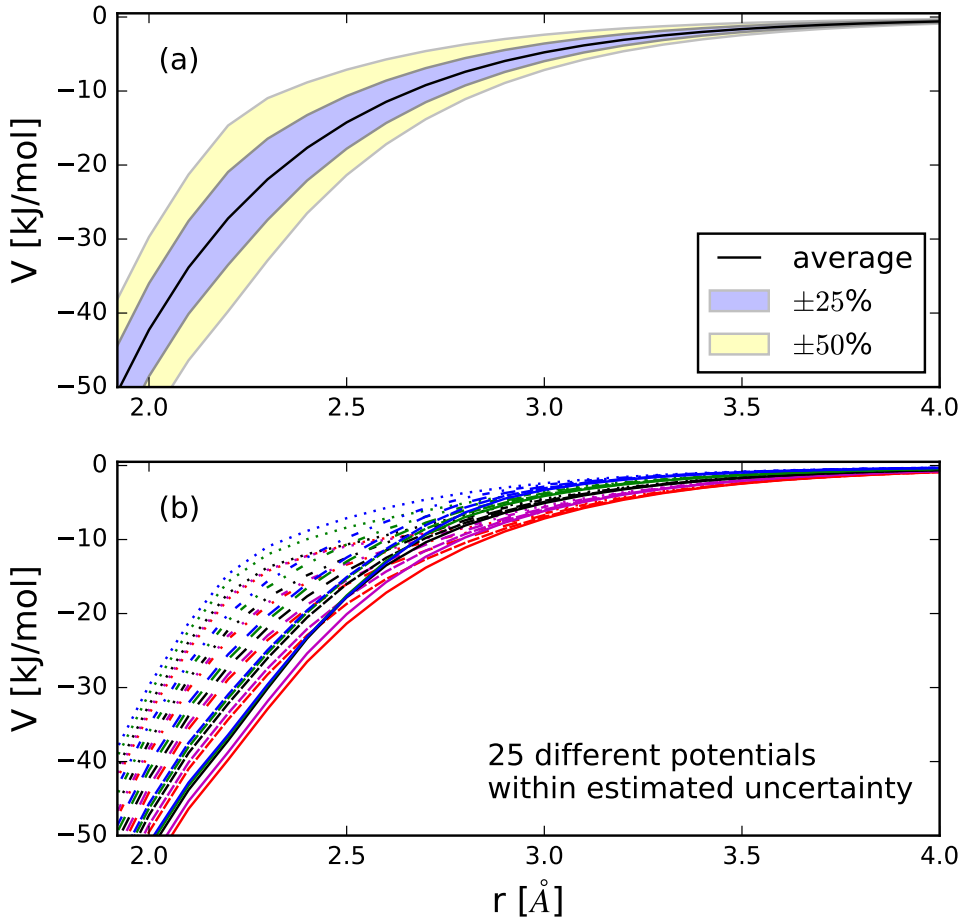

Figure 4: (a) minimum energy path between H + NO_2 and *syn*-HONO. The solid black line the the average potential of the four different methods. The shaded regions correspond to the 25% and 50% uncertainty regime. (b) The 25 scaled potentials generated according to the curves in Figure 2.

Figure 4a presents the minimum energy path between H + NO_2 → *syn*-HONO; the blue shaded region represents an uncertainty envelope of 25%, and the yellow region 50% uncertainty in the minimum energy path. The degree of convergence for this potential was the same as for the competing

$H + NO_2 \rightarrow HNO_2$ pathway, shown in Figure 3. Figure 4b illustrates the 25 $V_{\text{new}}(r)$ that are created from the scaling factors f in Figure 2.

3.2. OH + NO → products

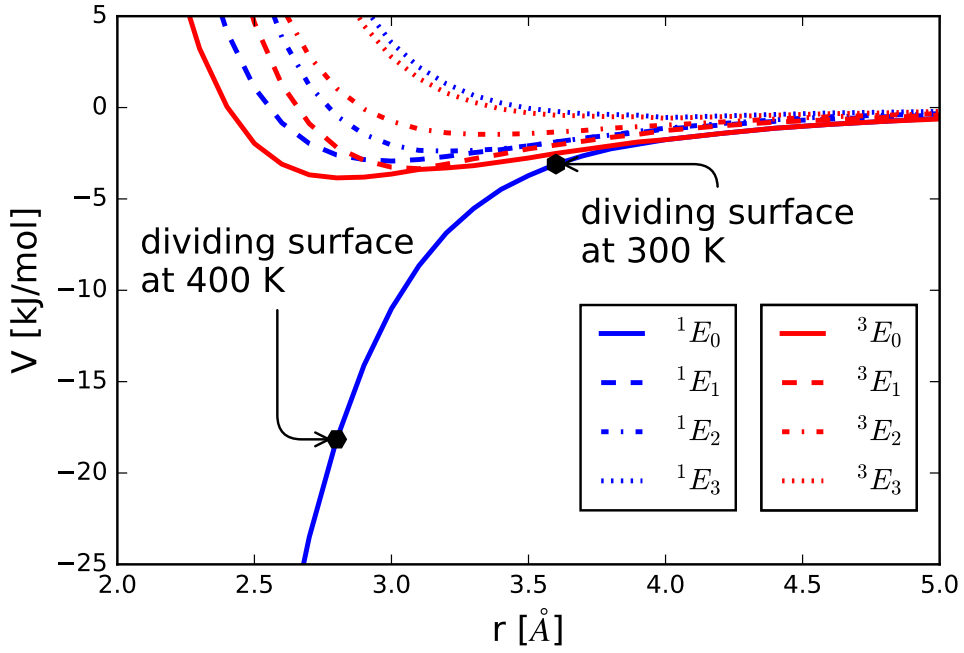

Figure 5: Interaction potentials for OH + NO as a function of the N−O distance. The blue curves correspond to the singlet surface, and the red curves the triplet. The broken lines are for the excited states for each electronic spin. The black hexagons indicate the location of the dividing surface on the ground state singlet as a function of temperature.

The results for the OH + NO interaction potential are shown in Figure 5. Proper calculation of the rate constant for OH + NO → HONO is complicated by non-adiabatic effects, with four states on the singlet surface (blue curves) and four states on the triplet surface (red). For $r \geq 3.5$ Å, all eight curves are attractive, but only the ground state singlet remains attractive

for $r \leq 2.4$ Å. A detailed analysis of the contribution of these higher states would require non-adiabatic dynamics simulations, which is beyond the scope of the present work. Further complications are spin-orbit effects and rovibronic coupling at lower temperatures. Instead, we note that these effects become increasingly irrelevant at higher temperatures.

To quantify the temperature at which these effects become negligible, we consider a limiting case in which the crossing from the excited electronic and spin states to the ground state singlet is rapid. In this approximation, the sum of the contributions to the interaction potential should be included prior to the variational optimization of the dividing surface. From the VRC-TST analysis, which used only the singlet ground state (solid blue line in Figure 5), we can obtain the location of the optimum dividing surface as a function of temperature. At 300 K, it is approximately $r = 3.6$ Å, and the contribution of the other surfaces is not insignificant (nearly a factor of three). As the temperature is increased, the optimum dividing surface shifts to shorter separation distances. By 400 K, the dividing surface is located at $r = 2.8$ Å; under these conditions, the contribution of the seven additional states is a mere 4%. This value likely is an over-estimate, since our strong-coupling assumption may be appropriate for the exited singlet states, but is less likely to be appropriate for the triplet surface. (The other limiting model is to assume that the crossing is slow, in which case the variational analysis is performed on each surface independently. Given that the other surfaces have local minima between -3.8 and -0.5 kJ/mol, their flux through the dividing surface will be comparatively negligible.) For these reasons, we do not include experimental data below 400 K in the optimization procedure,

since it would bias the result towards more attractive minimum energy paths. Instead, we restrict ourselves to the 400 K data of Fulle et al.

3.3. Optimized Mechanism

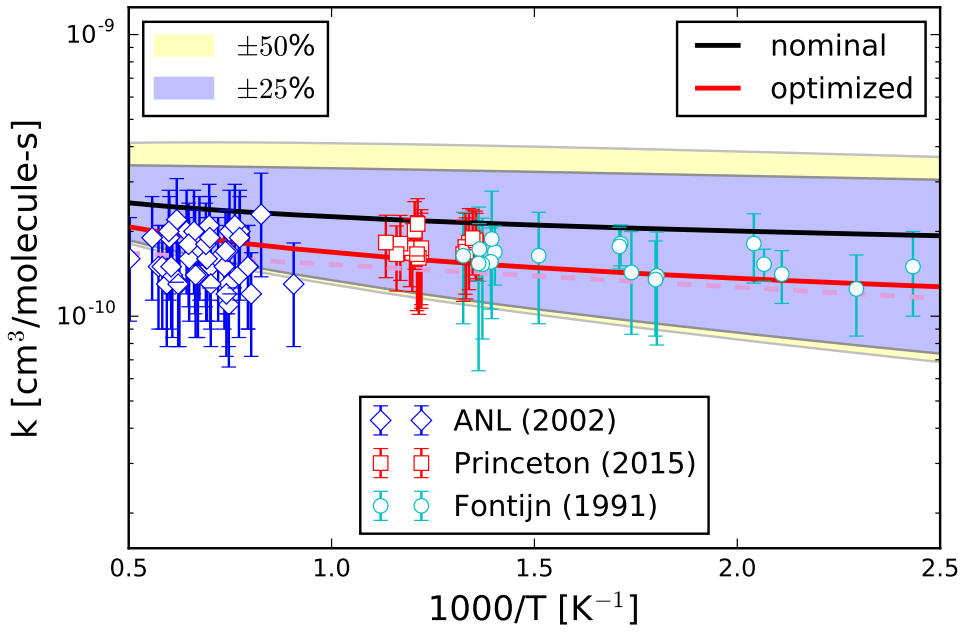

Figure 6: Rate constants for H + NO_2 → OH + NO. The symbols correspond to the experimental data: the blue diamonds are the high-temperature shock tube from ANL [48]; the red squares are the intermediate temperature flow tube from Princeton [47], and the cyan circles are the low-temperature flow cells of Fontjin [46]. The solid black line is the VRC-TST result for the nominal case, and the solid red line is the optimized result. The dashed magenta line is the linear least squares fit to the experimental data.

The optimized results for H + NO_2 → OH + NO are shown in Figure 6. The dashed line is a least squares fit to the experimental data (open symbols). The solid lines are the theoretical predictions, which includes the flux through both entrance channels (addition to N and O). The nominal

value (black line) corresponds to the unscaled result, which is higher than the least-squares fit by slightly less than a factor of two. As part of the optimization process, the barrier height for $HNO_2 \rightarrow$ anti-HONO was reduced from -93.9 to -96.4 kJ/mol (relative to H + NO_2). In terms of the scaling factors for the barrierless entrance channels: for H + $NO_2 \rightarrow$ *syn*-HONO, the optimized potential was 25% more attractive at close range, but unperturbed at long range (*e.g.* close-dash black in Figure 2); for H + $NO_2 \rightarrow HNO_2$, the optimized potential was unperturbed at close range, but was 25% less attractive at long range (*e.g.* wide-dash green in Figure 2). The H + NO_2 $\rightarrow$ OH + NO showed no sensitivity to collisional energy transfer variation, nor to the OH + NO minimum energy path. Note that the optimized result (red line) agrees with the experimental data to within 10%; thus, subtle changes to the curvature of the minimum energy path provide an impressive improvement to the final rate constant.

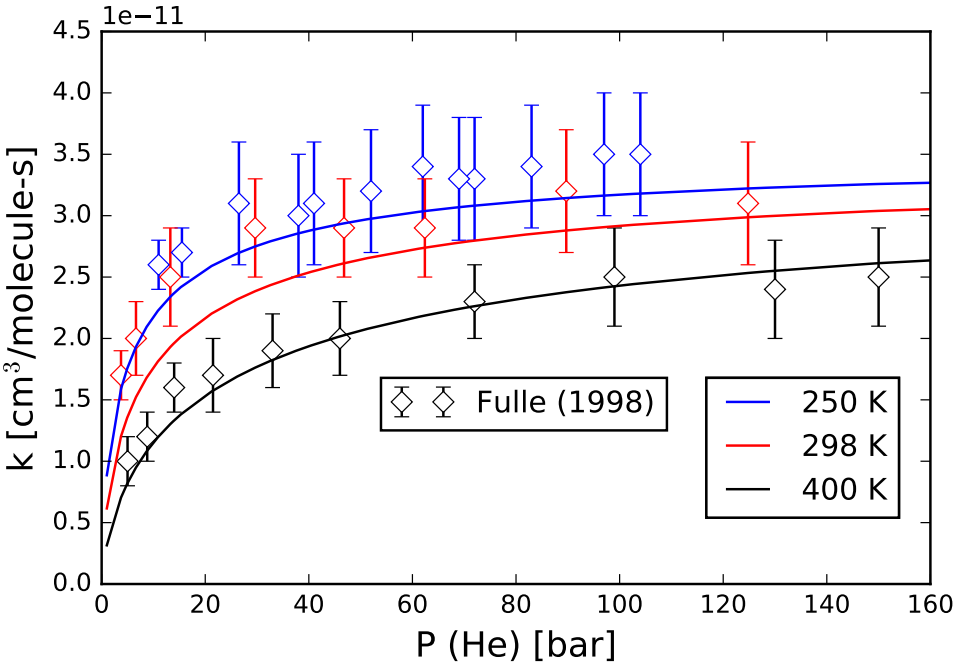

Figure 7: Rate constants for OH + NO → HONO. The symbols correspond to the data of Fulle et al. [49], and the solid lines are the optimized model predictions. Only the 400 K data (black) was used in the optimization process.

The optimized results for OH + NO → HONO are shown in Figure 7. The high-pressure data of Fulle [49] are an excellent compliment to the H + NO_2 data, since they provide constraints for both collisional energy transfer and OH + NO minimum energy path. The optimized result for the collisional energy transfer prefactor was $\langle \Delta E_{\text{down}} \rangle = 300\,(T/298[\text{K}])^{0.85}$ cm^{-1}. The OH + NO interaction potential was shifted up by a constant of 25% (*e.g.* dash-dot green in Figure 2). Note that even though only the data from 400 K (black symbols) were included in the optimization process, the lower termperature data are still well reproduced by the optimized model. The optimized rate

constant slightly under-predicts the experimental data at 250 and 298 K, which is consistent with our expectation that non-adiabatic effects will be important at lower temperatures.

3.4. Unimolecular kinetics

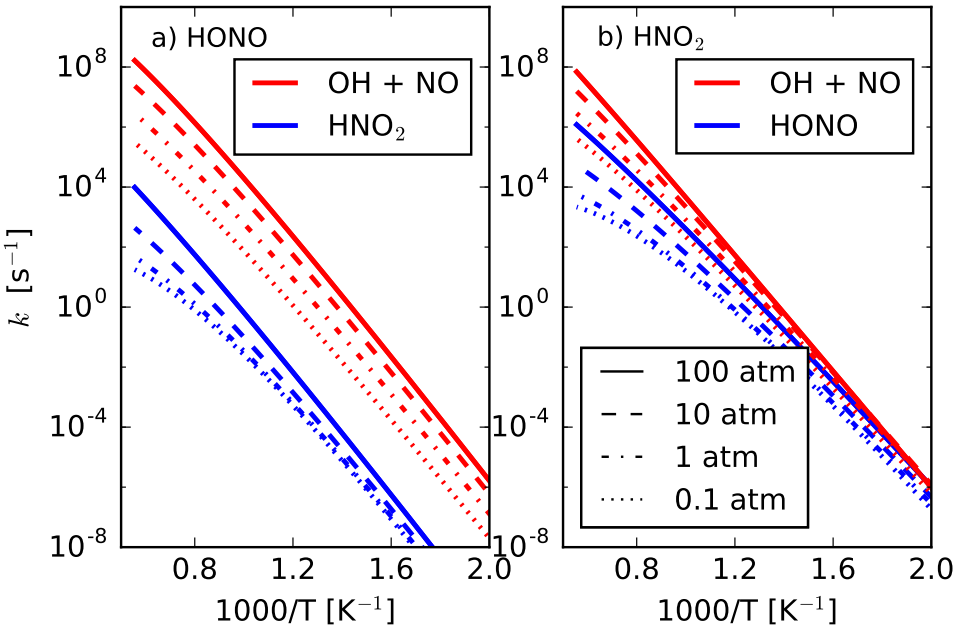

Figure 8: Rate constants for unimolecular decomposition (red) and isomerization (blue) for (a) HONO and (b) HNO_2. The different line styles correspond to different pressures. Decomposition to H + NO_2 is negligible.

The results for the decomposition of HONO and HNO_2 are shown in Figure 8. For HONO, Figure 8a, the only significant product is OH + NO, with isomerization to HNO_2 being four orders of magnitude smaller. This result is unsurprising, since, as seen in Figure 1, the OH + NO products are lower in energy than the barrier for isomerization to HNO_2, and thus the barrierless

decomposition is both enthalpically and entropically favorable at all temperatures. For HNO_2 decomposition, Figure 8b, thermally activated OH + NO also is the dominant product channel, with isomerization approximately two orders of magnitude smaller. For this product channel, as the population of HNO_2 isomerizes to HONO, the rate of collisional stabilization cannot compete with bond fission, and the vibrationally hot HONO intermediate promptly dissociates. Thus, isomerization between HONO and HNO_2 is, for all intents and purposes, negligible, with both isomers decomposing to OH + NO. Formation of H + NO_2 is negligible under all conditions.

3.5. Comparison with Literature Values

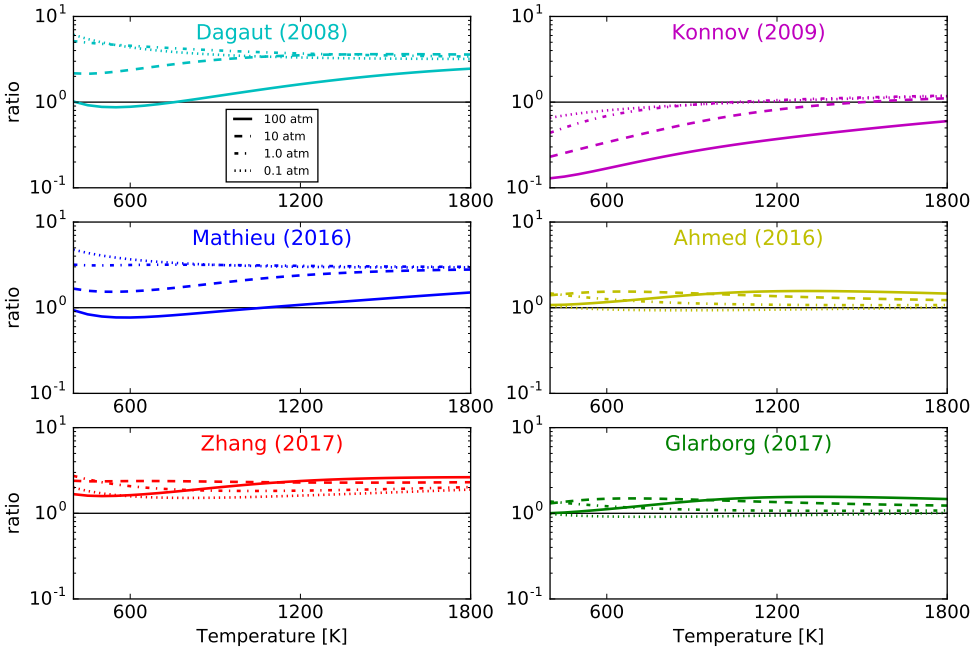

Figure 9: Ratio of literature values to the present work for the HONO → OH + NO rate constant. The line styles correspond to different pressures.

To assess the impact of the newly optimized $HONO/HNO_2$ mechanism on model predictions, we consider six different mechanisms that have been published in the past ten years: Daguat et al.[51], Konnov [52], Mathieu et al.[53], Ahmed et al.[54], Zhang et al.[10], and Glarborg et al. [6]. These mechanisms, along with the present work, were imported into CANTERA.[55] In all cases, the literature mechanisms represent the reaction in the association direction, OH + NO → HONO, with values taken from either Tsang and Herron[56] (Dagaut, Konnov, Mathieu) or Fulle et al.[49] (Ahmed, Zhang, Glarborg). In some cases, the Troe broadening factor F_{cent}[57] was modified by the authors. The largest source of discrepancy between the literature models, however, is due to the thermochemistry of OH, NO, and HONO, since the rate constant for HONO → OH + NO is computed using the equilibrium constant to maintain thermodynamic consistency. Nonetheless the agreement of the literature models with each other and with the present work is good, typically differing by less than an order of magnitude. The best agreement is with the Glarborg mechanism, which uses the ATcT thermochemistry, and is within a factor of two of the present work.

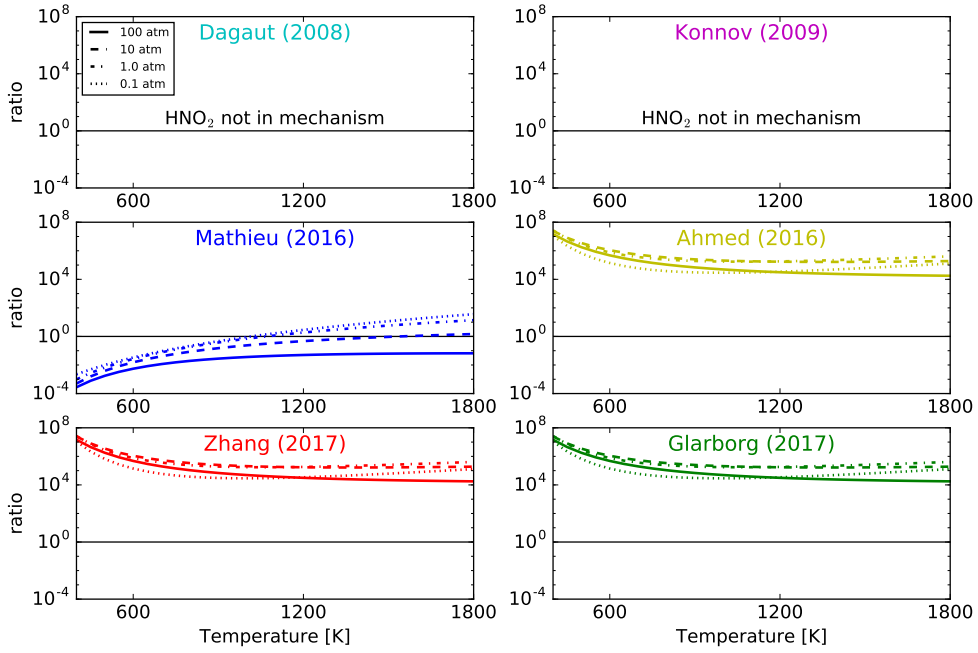

Figure 10: Ratio of literature values to the present work for the $HNO_2 \rightarrow$ HONO rate constant. The line styles correspond to different pressures.

For HNO_2 kinetics, however, the present work is significantly different from all prior mechanisms. Two of the mechanisms, Dagaut and Konnov, do not include HNO_2 as a distinct species. For the other four mechanisms, the only unimolecular reaction for HNO_2 is isomerization to HONO. The ratio of the literature values to the present work for $HNO_2 \rightarrow$ HONO are shown in 10. Here the published values differ by up to eight orders of magnitude. As demonstrated in Figure 8, the most important product channel for HNO_2 is the well skipping reaction to form OH + NO, but none of the previous mechanisms include this reaction. Instead, they tend to rely on early predictions of Dean and Bozzelli for HNO_2, which used QRRK and modified strong collision[5]. Importantly, that earlier work did not include OH + NO as a

possible channel and thus overestimated the rate collisional stabilization of HONO from HNO_2.

4. Conclusions

The HNO_2 potential energy surface is computed using post-coupled cluster methods, with an uncertainty of ± 1.3 kJ/mol. For the barrierless reactions, the minimum energy paths are computed using different multi-reference methods. Temperature- and pressure-dependent rate constants for HONO and HNO_2 are computed using microcanonical rate theory and the master equation. A novel strategy was developed to incorporate uncertainty in the minimum energy pathway into the optimized mechanism. The new mechanism is in excellent agreement with all available experimental data for $H + NO_2 \rightarrow OH + NO$ and $OH + NO \rightarrow HONO$. This work highlights the importance of well-skipping reactions, with OH + NO being the most important product channel for HNO_2, even though all prior literature mechanisms for HNO_2 failed to include this pathway. The resulting HONO and HNO_2 mechanism, coupled with the uncertainty analysis, is expected to provide important constraints on future mechanism development for gas-phase nitrogen chemistry.

Conflicts of interest

There are no conflicts to declare.

Acknowledgements

The authors would like to thank Stephen Klippenstein, Lawerence Harding, and Ahren Jasper of Argonne National Laboratory for many helpful discussions on variational transition state theory, electronic structure methods, and nonadiabatic dynamics. MEF gratefully acknowledges support by the U.S. National Science Foundation through Award Number CBET-1553366, with Dr. Song-Charng Kong as the program manager. XC gratefully acknowledges support by the U.S. Office of Naval Research through ONR Grant Number N00014-1-61-2054, with Dr. Chad Stoltz as the program manager. CFG gratefully acknowledges the NSF, ONR, and Brown University for support on this project.

References

[1] A. M. Ickes, S. V. Bohac, D. N. Assanis, Effect of 2-ethylhexyl nitrate cetane improver on NO_x emissions from premixed low-temperature diesel combustion, Energy & Fuels 23 (10) (2009) 4943–4948. doi:10.1021/ef900408e.

[2] A. B. Dempsey, N. R. Walker, R. D. Reitz, Effect of cetane improvers on gasoline, ethanol, and methanol reactivity and the implications for RCCI combustion, SAE Int. J. Fuels Lubr. 6 (1) (2013) 170–187. doi:10.4271/2013-01-1678.

[3] D. A. Splitter, R. D. Reitz, Fuel reactivity effects on the efficiency and operational window of dual-fuel compression ignition engines, Fuel 118 (2014) 163–175. doi:10.1016/j.fuel.2013.10.045.

[4] J. A. Miller, C. T. Bowman, Mechanism and modeling of nitrogen chemistry in combustion, Progress in Energy and Combustion Science 15 (4) (1989) 287 – 338. doi:10.1016/0360-1285(89)90017-8.

[5] A. M. Dean, J. W. Bozzelli, Combustion Chemistry of Nitrogen, Springer New York, New York, NY, 2000, Ch. 2, pp. 125–341.

[6] P. Glarborg, J. A. Miller, B. Ruscic, S. J. Klippenstein, Modeling nitrogen chemistry in combustion, Prog. Energy Combust. Sci. 67 (2018) 31–68.

[7] O. Mathieu, A. Levacque, E. Petersen, Effects of NO_2 addition on hydrogen ignition behind reflected shock waves, Proceedings of the Combustion Institute 34 (1) (2013) 633–640. doi:10.1016/j.proci.2012.05.067.

[8] P. Gokulakrishnan, C. C. Fuller, M. S. Klassen, R. G. Joklik, Y. N. Kochar, S. N. Vaden, T. C. Lieuwen, J. M. Seitzman, Experiments and modeling of propane combustion with vitiation, Combustion and Flame 161 (8) (2014) 2038 – 2053. doi:https://doi.org/10.1016/j.combustflame.2014.01.024.

[9] O. Mathieu, J. M. Pemelton, G. Bourque, E. L. Petersen, Shock-induced ignition of methane sensitized by NO_2 and N_2O, Combust. Flame 162 (8) (2015) 3053–3070. doi:10.1016/j.combustflame.2015.03.024.

[10] Y. Zhang, O. Mathieu, E. L. Petersen, G. Bourque, H. J. Curran, Assessing the predictions of a NOx kinetic mechanism on recent hydrogen and syngas experimental data, Combust. Flame 182 (2017) 122–141. doi:10.1016/j.combustflame.2017.03.019.

[11] M. E. Fuller, C. F. Goldsmith, On the modeling implications of treating HONO and HNO_2 as distinct chemical species in combustion, Proc. Comb. Inst. 37, accepted for publication.

[12] J. Chai, C. F. Goldsmith, Rate coefficients for fuel + NO_2 : Predictive kinetics for HONO and HNO_2 formation, Proc. Comb. Inst. 36 (1) (2017) 617–626. doi:10.1016/j.proci.2016.06.133.

[13] S. J. Klippenstein, L. B. Harding, B. Ruscic, Ab initio computations and active thermochemical tables hand in hand: Heats of formation of core combustion species, The Journal of Physical Chemistry A 121 (2017) 6580–6602.

[14] H.-J. Werner, Third-order multireference perturbation theory the CASPT3 method, Molecular Physics 89 (2) (1996) 645–661.

[15] P. Celani, H.-J. Werner, Multireference perturbation theory for large restricted and selected active space reference wave functions, The Journal of Chemical Physics 112 (13) (2000) 5546–5557.

[16] B. O. Roos, K. Andersson, Multiconfigurational perturbation theory with level shift - the Cr_2 potential revisited, Chemical Physics Letters 245 (2-3) (1995) 215–223.

[17] H.-J. Werner, P. J. Knowles, An efficient internally contracted multiconfiguration–reference configuration interaction method, The Journal of Chemical Physics 89 (9) (1988) 5803–5814.

[18] P. J. Knowles, H.-J. Werner, An efficient method for the evaluation of coupling coefficients in configuration interaction calculations, Chemical Physics Letters 145 (6) (1988) 514–522.

[19] S. R. Langhoff, E. R. Davidson, Configuration interaction calculations on the nitrogen molecule, International Journal of Quantum Chemistry 8 (1) (1974) 61–72.

[20] L. B. Harding, S. J. Klippenstein, H. Lischka, R. Shepard, Comparison of multireference configuration interaction potential energy surfaces for H + O_2 → HO_2: the effect of internal contraction, Theoretical Chemistry Accounts 133 (2) (2013) 1429. doi:10.1007/s00214-013-1429-6.

[21] C. F. Goldsmith, L. B. Harding, Y. Georgievskii, J. A. Miller, S. J. Klippenstein, Temperature and pressure-dependent rate coefficients for

the reaction of vinyl radical with molecular oxygen, Journal of Physical Chemistry A 119 (28) (2015) 7766–79.

[22] C. P. Moradi, A. M. Morrison, S. J. Klippenstein, C. F. Goldsmith, G. E. Douberly, Propargyl + O_2 reaction in helium droplets: Entrance channel barrier or not?, The Journal of Physical Chemistry A 117 (50) (2013) 13626–13635.

[23] X. Chen, C. F. Goldsmith, A Theoretical and Computational Analysis of the Methyl-Vinyl + O_2 Reaction and Its Effects on Propene Combustion, The Journal of Physical Chemistry A 121 (48) (2017) 9173–9184.

[24] H.-J. Werner, P. J. Knowles, G. Knizia, F. R. Manby, M. Schütz, P. Celani, W. Györffy, D. Kats, T. Korona, R. Lindh, A. Mitrushenkov, G. Rauhut, K. R. Shamasundar, T. B. Adler, R. D. Amos, A. Bernhardsson, A. Berning, D. L. Cooper, M. J. O. Deegan, A. J. Dobbyn, F. Eckert, E. Goll, C. Hampel, A. Hesselmann, G. Hetzer, T. Hrenar, G. Jansen, C. Köppl, Y. Liu, A. W. Lloyd, R. A. Mata, A. J. May, S. J. McNicholas, W. Meyer, M. E. Mura, A. Nicklass, D. P. O'Neill, P. Palmieri, D. Peng, K. Pflüger, R. Pitzer, M. Reiher, T. Shiozaki, H. Stoll, A. J. Stone, R. Tarroni, T. Thorsteinsson, M. Wang, Molpro, version 2015.1, a package of ab initio programs, see http://www.molpro.net (2015).

[25] M. J. Frisch, G. W. Trucks, H. B. Schlegel, G. E. Scuseria, M. A. Robb, J. R. Cheeseman, G. Scalmani, V. Barone, G. A. Petersson, H. Nakatsuji, X. Li, M. Caricato, A. V. Marenich, J. Bloino, B. G. Janesko, R. Gomperts, B. Mennucci, H. P. Hratchian, J. V. Ortiz, A. F. Izmaylov,

J. L. Sonnenberg, D. Williams-Young, F. Ding, F. Lipparini, F. Egidi, J. Goings, B. Peng, A. Petrone, T. Henderson, D. Ranasinghe, V. G. Zakrzewski, J. Gao, N. Rega, G. Zheng, W. Liang, M. Hada, M. Ehara, K. Toyota, R. Fukuda, J. Hasegawa, M. Ishida, T. Nakajima, Y. Honda, O. Kitao, H. Nakai, T. Vreven, K. Throssell, J. A. Montgomery, Jr., J. E. Peralta, F. Ogliaro, M. J. Bearpark, J. J. Heyd, E. N. Brothers, K. N. Kudin, V. N. Staroverov, T. A. Keith, R. Kobayashi, J. Normand, K. Raghavachari, A. P. Rendell, J. C. Burant, S. S. Iyengar, J. Tomasi, M. Cossi, J. M. Millam, M. Klene, C. Adamo, R. Cammi, J. W. Ochterski, R. L. Martin, K. Morokuma, O. Farkas, J. B. Foresman, D. J. Fox, Gaussian09 Revision D.01, Gaussian Inc. Wallingford CT (2013).

[26] Y. Georgievskii, J. A. Miller, M. P. Burke, S. J. Klippenstein, Reformulation and solution of the master equation for multiple-well chemical reactions, The Journal of Physical Chemistry A 117 (46) (2013) 12146–12154.

[27] Y. Georgievskii, S. J. Klippenstein, MESS: Master equation system solver 2016.3.23, `http://tcg.cse.anl.gov/papr/codes/mess.html/`.

[28] Y. Georgievskii, J. A. Miller, M. P. Burke, S. J. Klippenstein, PAPR: Predictive automated phenomenological rates v1, `http://tcg.cse.anl.gov/papr/`.

[29] K. P. Huber, G. Herzberg, Constants of diatomic molecules, Springer US, Boston, MA, 1979, pp. 8–689. doi:10.1007/978-1-4757-0961-22.

[30] B. Widom, Molecular transitions and chemical reaction rates, Science 148 (1965) 1555–1560. doi:10.1126/science.148.3677.1555.

[31] J. A. Miller, S. J. Klippenstein, Master equation methods in gas phase chemical kinetics, The Journal of Physical Chemistry A 110 (36) (2006) 10528–10544.

[32] J. A. Miller, S. J. Klippenstein, S. H. Robertson, M. J. Pilling, R. Shannon, J. Zador, A. W. Jasper, C. F. Goldsmith, M. P. Burke, Comment on "when rate constants are not enough", Journal of Physical Chemistry A 120 (2016) 306–312. doi:10.1021/acs.jpca.5b06025.

[33] C. F. Goldsmith, W. H. Green, S. J. Klippenstein, Role of O_2 + QOOH in Low-Temperature Ignition of Propane. 1. Temperature and Pressure Dependent Rate Coefficients, Journal of Physical Chemistry A 116 (13) (2012) 3325–3346. doi:10.1021/jp210722w.

[34] S. J. Klippenstein, R. A. Marcus, High pressure rate constants for unimolecular dissociation/free radical recombination: Determination of the quantum correction via quantum monte carlo path integration, The Journal of Chemical Physics 87 (6) (1987) 3410.

[35] S. J. Klippenstein, Variational optimizations in the rice-ramsperger-kassel-marcus theory calculations for unimolecular dissociations with no reverse barrier, The Journal of Chemical Physics 96 (1) (1992) 367–367.

[36] S. J. Klippenstein, The evaluation of N_e(R) within a variably defined reaction coordinate framework, Chemical Physics Letters 214 (3-4) (1993) 418–424.

[37] S. J. Klippenstein, An efficient procedure for evaluating the number of available states within a variably defined reaction coordinate framework, Journal of Physical Chemistry 98 (1994) 11459–11464.

[38] Y. Georgievskii, S. J. Klippenstein, Variable reaction coordinate transition state theory: Analytic results and application to the C_2H_3 + H $\rightarrow$ C_2H_4 reaction, The Journal of Chemical Physics 118 (12) (2003) 5442–5442.

[39] Y. Georgievskii, S. J. Klippenstein, Transition state theory for multichannel addition reactions: Multifaceted dividing surfaces, The Journal of Physical Chemistry A 107 (46) (2003) 9776–9781.

[40] D. McQuarrie, Statistical Mechanics, University Science Books, 2000.

[41] J. A. Miller, S. J. Klippenstein, From the multiple-well master equation to phenomenological rate coefficients: reactions on a C_3H_4 potential energy surface, The Journal of Physical Chemistry A 107 (15) (2003) 2680–2692. doi:10.1021/jp0221082.

[42] M. P. Burke, S. J. Klippenstein, L. B. Harding, A quantitative explanation for the apparent anomalous temperature dependence of OH+HO_2=H_2O+O_2 through multi-scale modeling, Proceedings of the Combustion Institute 34 (1) (2013) 547 – 555. doi:10.1016/j.proci.2012.05.041.

[43] M. P. Burke, C. F. Goldsmith, S. J. Klippenstein, O. Welz, H. Huang, I. O. Antonov, J. D. Savee, D. L. Osborn, J. Zdor, C. A. Taatjes, L. Sheps, Multiscale informatics for low-temperature propane

oxidation: Further complexities in studies of complex reactions, The Journal of Physical Chemistry A 119 (28) (2015) 7095–7115. doi:10.1021/acs.jpca.5b01003.

[44] O. Welz, M. P. Burke, I. O. Antonov, C. F. Goldsmith, J. D. Savee, D. L. Osborn, C. A. Taatjes, S. J. Klippenstein, L. Sheps, New insights into low-temperature oxidation of propane from synchrotron photoionization mass spectrometry and multiscale informatics modeling, The Journal of Physical Chemistry A 119 (28) (2015) 7116–7129. doi:10.1021/acs.jpca.5b01008.

[45] M. P. Burke, Harnessing the combined power of theoretical and experimental data through multiscale informatics, International Journal of Chemical Kinetics 48 (4) (2016) 212–235. doi:10.1002/kin.20984.

[46] T. Ko, A. Fontijn, High-temperature photochemistry kinetics study of the reaction H + NO_2 → OH + NO from 296 to 760 K, The Journal of Physical Chemistry 95 (10) (1991) 3984–3987. doi:10.1021/j100163a019.

[47] F. M. Haas, F. L. Dryer, Rate coefficient determinations for H + NO_2 → OH + NO from high pressure flow reactor measurements, The Journal of Physical Chemistry A 119 (28) (2015) 7792–7801. doi:10.1021/acs.jpca.5b01231.

[48] M.-C. Su, S. S. Kumaran, K. P. Lim, J. V. Michael, A. F. Wagner, L. B. Harding, D.-C. Fang, Rate constants, 1100 ≤ T ≤ 2000 K, for H + NO_2 → OH + NO using two shock tube techniques: Comparison of theory

to experiment, The Journal of Physical Chemistry A 106 (36) (2002) 8261–8270. doi:10.1021/jp0141023.

[49] D. Fulle, H. F. Hamann, H. Hippler, J. Troe, Temperature and pressure dependence of the addition reactions of HO to NO and to NO_2. IV. saturated laser-induced fluorescence measurements up to 1400 bar, The Journal of Chemical Physics 108 (13) (1998) 5391–5397. doi:10.1063/1.475971.

[50] B. Ruscic, D. H. Bross, Active thermochemical tables (ATcT) values based on ver. 1.122 of the thermochemical network., `https://atct.anl.gov/`.

[51] P. Dagaut, P. Glarborg, M. Alzueta, The oxidation of hydrogen cyanide and related chemistry, Prog. Energy Combust. Sci. 34 (1) (2008) 1–46. doi:10.1016/j.pecs.2007.02.004.

[52] A. Konnov, Implementation of the NCN pathway of prompt-NO formation in the detailed reaction mechanism, Combust. Flame 156 (11) (2009) 2093–2105. doi:10.1016/j.combustflame.2009.03.016.

[53] O. Mathieu, B. Giri, A. Agard, T. Adams, J. Mertens, E. Petersen, Nitromethane ignition behind reflected shock waves: Experimental and numerical study, Fuel 182 (2016) 597–612. doi:10.1016/j.fuel.2016.05.060.

[54] S. F. Ahmed, J. Santner, F. L. Dryer, B. Padak, T. I. Farouk, Computational study of NO_x formation at conditions relevant to gas turbine operation, part 2: NO_x in high hydrogen content fuel combus-

tion at elevated pressure, Energy & Fuels 30 (9) (2016) 7691–7703. doi:10.1021/acs.energyfuels.6b00421.

[55] D. G. Goodwin, H. K. Moffat, R. L. Speth, Cantera: An object-oriented software toolkit for chemical kinetics, thermodynamics, and transport processes, `http://www.cantera.org`, version 2.2.1 (2016).

[56] W. Tsang, J. T. Herron, Chemical kinetic data base for propellant combustion i. reactions involving NO, NO_2, HNO, HNO_2, HCN and N_2O, J. Phys. Chem. Ref. Data 20 (4) (1991) 609–663. doi:10.1063/1.555890.

[57] R. G. Gilbert, K. Luther, J. Troe, Theory of thermal unimolecular reactions in the fall-off range. ii. weak collision rate constants, Berichte der Bunsengesellschaft fur physikalische Chemie 87 (2) (1983) 169–177. doi:10.1002/bbpc.19830870218.